Surface-induced contraction mechanism of basal plane dislocations in 4H-SiC: Dislocation dynamics analysis

Atsuo Hirano,* Noboru Takahashi, and Akiyuki Takahashi
Tokyo University of Science, 2641 Yamazaki, Noda, Chiba 278-8510, Japan

(Received 30 April 2026; revised 16 October 2026; accepted 28 October 2026; published 12 November 2026)

Basal plane dislocations (BPDs) in the epitaxial layer in 4H-SiC is one of the remarkable manufacturing issues because they degrade device performance. Although most BPDs are converted to threading edge dislocations (TEDs), some remain. Therefore, elucidating the mechanism of BPD-TED conversion is crucial for the enhancement of this process. In this study, we addressed this gap by analytically clarifying the contraction mechanism of partial BPDs, which is one of the main processes in BPD-TED conversion. We employed the dislocation dynamics method based on dislocation theories, which can precisely describe interactions between dislocations. Our method incorporates surface effects such as image force in addition to the elastic interaction between dislocations and stacking faults by calculating the stress derived from the surface. Using this method, we focused on the effect of a terrace and step riser comprising steps on the epitaxial surface. The results revealed that the depth of the BPD pair from the surface as well as the direction of the Burgers vectors relative to the step riser significantly influence the contraction of BPDs. In addition, we investigated a model with an off-angle to determine its effect on BPD contraction, which showed that the BPD width decreases for small off-angles and closed Burgers vectors. Therefore, a small off-angle can result in a high BPD-TED conversion rate, which is consistent with the experimental results. These findings were clearly explained by the forces exerted on dislocations by the surface-induced stress. Our computational model clarifies the mechanism of BPD-TED conversion and is expected to be applicable to other SiC epitaxy conditions.

DOI: 10.1103/rz4d-3yjc

I. INTRODUCTION

4H-SiC, referred to as "SiC" in this study, exhibits superior electrical properties such as a high voltage resistance and a low on-resistance compared with silicon [1]. Consequently, SiC has been used in various devices such as inverters, transistors, and diodes as a new-generation material [2,3]. During the manufacturing process of SiC wafers, the chemical vapor deposition (CVD) method is used for epitaxial growth to enhance wafer quality [4,5]. Because defects can degrade device performance [6–10], processes for eliminating them have been extensively studied [8,11–14]. One of the most harmful defects in SiC devices is basal plane dislocations (BPDs), which exist on the basal plane in the form of dissolved partial dislocations in SiC. Stacking faults between BPDs can easily expand, resulting in device degradations, such as bipolar degradation [15,16], because BPDs have a high mobility. Most BPDs are converted to threading edge dislocations (TEDs) during epitaxial growth owing to the step-controlled epitaxy [4,17], which has the same Burgers vector as BPDs but different dislocation directions and does not affect device performance [18] in the epitaxial layer (BPD-TED conversion) [19–21]. However, some BPDs that degrade device performance remain [18]. Therefore, eliminating the BPDs in the epitaxial layer is crucial for enhancing the BPD-TED conversion. Several experimental methods have been suggested to improve the BPD-TED conversion rate, such as growth off-angles [22,23], growth velocities [13,14,24,25], and temperature [26], and others [27–30]. For example, a lower BPD density can be achieved using 4 ° off-angle substrates compared with 8 ° off-angle ones [22,23].

However, the BPD-TED conversion mechanism remains unclear, although some computational studies have been performed. For instance, first-principles calculations, such as density functional theory (DFT) and density functional-based tight-binding (DFTB) calculations, have been used to calculate double kink formation energies, which affect the mobility of dislocations, and structures around BPD cores [31–35]. However, they cannot be applied directly to BPD-TED conversion, whose analysis requires the simulation of a large number of atoms, because they can only be used for small atomic volumes (∼10 000 atoms). Previous studies also used classical molecular dynamics (MD). Because the interactions between atoms are calculated using empirical interatomic potentials, MD can handle significantly more atoms than first-principles calculations. Therefore, it can be used to treat structures with large strain fields generated by dislocations. A previous study using the existing interatomic potential concluded that BPDs can be easily converted to TEDs near the surface shortly after two partial BPDs contract to a

*Contact author: hirano.atsuo@rs.tus.ac.jp

Published by the American Physical Society under the terms of the Creative Commons Attribution 4.0 International license. Further distribution of this work must maintain attribution to the author(s) and the published article's title, journal citation, and DOI.

perfect BPD [36]. Another study developed a new interatomic potential for SiC to reproduce the dislocation motion near the surface and clarified that partial BPDs in the vicinity of the surface can easily contract into a perfect dislocation [37,38] by calculating dislocation mobilities. However, MD cannot be used for mesoscale (∼nm–μm scale) phenomena because it requires a significant number of atoms for modeling. In addition, no interatomic potential still can reproduce the dislocations in SiC with a high accuracy. For instance, the stacking fault energy calculated using previously developed interatomic potentials [37] is approximately 1.1 $\mathrm{mJ/m^2}$ whereas that calculated experimentally is approximately 15 $\mathrm{mJ/m^2}$ [39–41]. Therefore, a new computational method for SiC dislocations that can handle mesoscale models with a high accuracy is desired.

BPDs are usually dissociated into Shockley-type partial dislocation pairs [42], which are considered to contract in the vicinity of the surface and are converted into TEDs [19,21,43]. The previous MD study concluded that BPDs can be easily converted to TEDs near the surface shortly after two partial BPDs contract to a perfect BPD [36], which indicates that the contraction of partial BPDs is crucial process for BPD-TED conversion. Therefore, in this study, we focused on the process of the contraction of two partial BPDs, which has not been completely clarified. We address the existing gap by applying the dislocation dynamics (DD) method as an alternative to the MD method to enable mesoscale investigations of BPD-TED conversion. Dislocations are directly modeled in DD simulations, whereas they are modeled by arranging atoms in MD. Therefore, DD simulations can handle larger-scale phenomena than MD. In addition, the interactions between dislocations are determined based on the elasticity theory of dislocations in DD simulations, whereas they depend on an interatomic potential in MD. Therefore, by correctly implementing the elasticity theory of dislocations and the surface effect in DD simulations, DD simulations are expected to reproduce dislocations near the surface with a high accuracy. Several methods are available for treating near-surface dislocations using DD simulations. For instance, some researchers have suggested that image dislocations were set to satisfy a surface traction of zero [44,45]. Others suggested that image stresses were implemented on the surface [46,47]. We used the latter method because it can easily treat screw and edge dislocations in two- and three-dimensional models. Using this method, we elucidated the effect of the surface on the dislocation behaviors in SiC. Since the dislocation behavior near surface is governed by complex interactions, we believe that DD provides an effective framework for their behavior.

The pairs of partial BPDs can be categorized into three types: 30 °C core–30 ° Si core pair, 30 °C core–90 °C core pair, and 30 ° Si core–90 ° Si core pair. The movement of dislocations depends on the type of partial dislocation. For instance, the 30 °C core–30 ° Si core pair remains in the epitaxial layer, whereas the 30 °C core–90 °C core and 30 ° Si core–90 ° Si core pairs do not [14,48]. In addition, 90 ° partial dislocations move more freely compared with 30 ° partial dislocations [31,33]. Therefore, we focused on the behavior of these partial dislocations near the surface. Moreover, the step-controlled epitaxy produces steps on the surface with heights of 0.25–1.0 nm [4]. In this study, we define

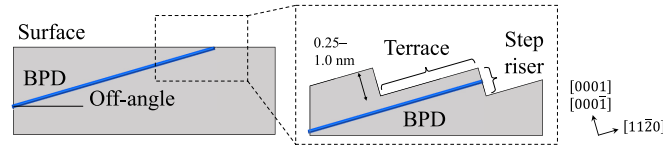


FIG. 1. Schematic of the surface in the epitaxial layer and its enlarged view. The blue line shows a BPD on the basal plane. The terrace and step riser are defined in this study as the surface on the basal plane and the vertical surface connecting adjacent terraces, respectively.

"terrace" as the surface on the basal plane and "step riser" as the vertical surface connecting adjacent terraces, as shown in Fig. 1. We considered the effects of terraces and step risers on BPD movement. Using our DD method, we elucidated the movements of various types of partial BPD pairs, particularly BPD contractions, near the epitaxial surface.

Section II presents the details of the proposed DD method. In Sec. III, we clarify the effect of terraces on the BPD pair configurations using a two-dimensional model. In addition, we present the results and discuss the calculations. Subsequently, in Sec. IV, we show the effect of step risers on the BPD pair configurations using a three-dimensional model. As our analysis integrates the effects of terraces and step risers, we clarified the off-angle effect on BPD contraction near the surface using a model with an off-angle in Sec. V. Finally, Sec. VI presents our conclusions.

II. METHODOLOGY

In this section, we describe the computational method. Here, we consider two straight, partial BPDs, i.e., dislocations (1) and (2), with width w at depth d from the surface, as shown in Fig. 2. The force at a point on each dislocation can be calculated as

$$\boldsymbol{f} = \boldsymbol{f}_{\mathrm{SF}} + \boldsymbol{f}_{\mathrm{PK}}, \tag{1}$$

where $\boldsymbol{f}_{\mathrm{SF}}$ is the force generated by the stacking fault, and $\boldsymbol{f}_{\mathrm{PK}}$ is the Peach-Koehler force acting on the dislocation. $\boldsymbol{f}_{\mathrm{SF}}$ and $\boldsymbol{f}_{\mathrm{PK}}$ correspond to the attractive and repulsive forces between two dislocations, respectively.

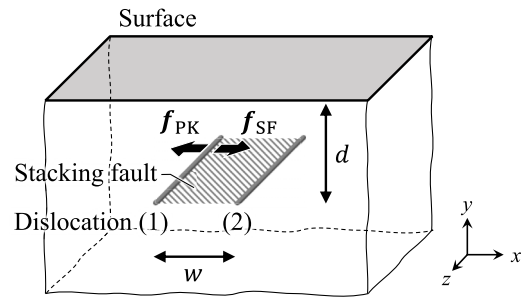


FIG. 2. Schematic of two partial dislocations (1) and (2) with width w below a distance d from the surface. Note that the dislocation lines are assumed to be infinite when a two-dimensional model is employed.

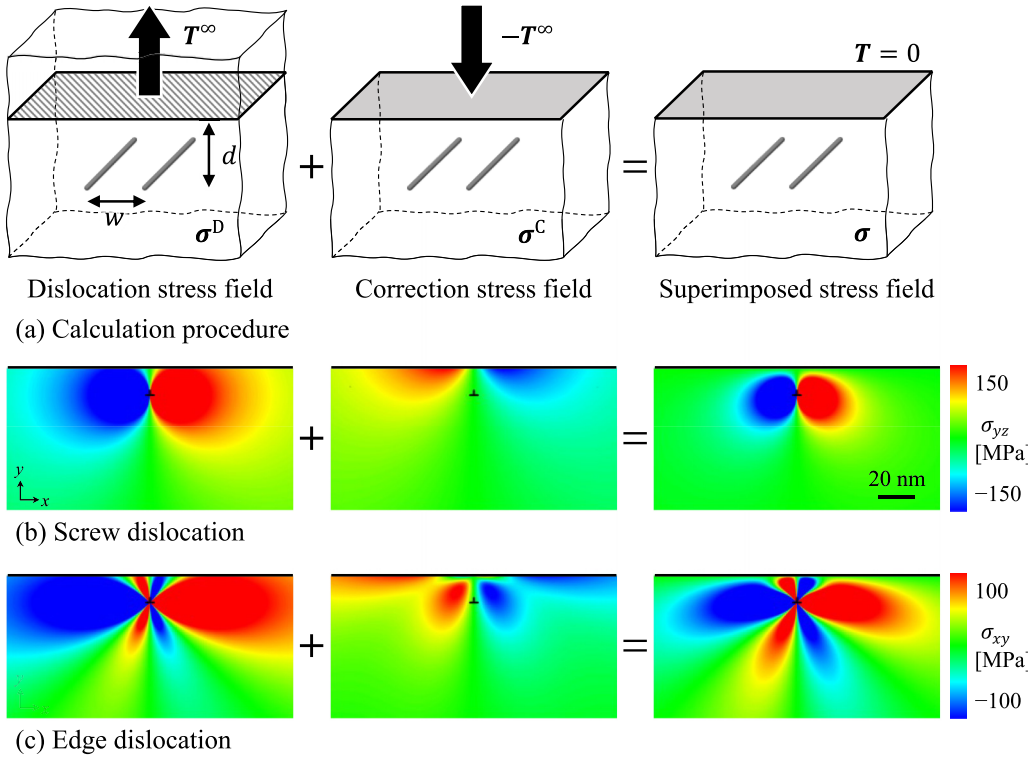


FIG. 3. Dislocation, correction, and superimposed stress fields near the surface. (a) Calculation procedure. (b) σ_{yz} of each stress field around a screw dislocation. (c) σ_{xy} around an edge dislocation. The dislocation with a Burgers vector magnitude of 0.1782 nm is $d = 15$ nm below the surface, and the model is large enough in the x and y directions in panels (b), (c).

Force $\boldsymbol{f}_{\mathrm{SF}}$ per unit length is calculated using the stacking fault energy Γ as follows:

$$|\boldsymbol{f}_{\mathrm{SF}}| = \Gamma. \tag{2}$$

The direction of $\boldsymbol{f}_{\mathrm{SF}}$ depends on the positions of the dislocation lines and stacking faults.

Force $\boldsymbol{f}_{\mathrm{PK}}$ at a point on the dislocation can be calculated as

$$\boldsymbol{f}_{\mathrm{PK}} = \boldsymbol{\sigma} \cdot \boldsymbol{b} \times \boldsymbol{t}, \tag{3}$$

where $\boldsymbol{\sigma}$, $\boldsymbol{b}$, and $\boldsymbol{t}$ are stresses acting on the dislocation segment, the Burgers vector, and the tangent vector of the dislocation segment, respectively. Stress $\boldsymbol{\sigma}$ comprises two stresses as follows:

$$\boldsymbol{\sigma} = \boldsymbol{\sigma}^{\mathrm{D}} + \boldsymbol{\sigma}^{\mathrm{C}}. \tag{4}$$

$\boldsymbol{\sigma}^{\mathrm{D}}$ is the stress generated from dislocations, and $\boldsymbol{\sigma}^{\mathrm{C}}$ is the stress derived from the surface called the correction stress in this study.

Figure 3(a) shows the schematic of the calculation procedure of the correction stress field $\boldsymbol{\sigma}^{\mathrm{C}}$. First, the stress $\boldsymbol{\sigma}^{\mathrm{D}}$ generated by all dislocations is obtained using the dislocation theory in the infinite body. The force $\boldsymbol{T}^\infty$ in the surface position is calculated using the dislocation stress field. Subsequently, the correction stress field $\boldsymbol{\sigma}^{\mathrm{C}}$ can be calculated by applying the force $-\boldsymbol{T}^\infty$ on the surface Others suggested that image stress should be implemented on the surface because the surface traction $\boldsymbol{T}$ on the surface must be zero. In this study, we employed our in-house finite element (FE) code to calculate $\boldsymbol{\sigma}^{\mathrm{C}}$. Figures 3(b) and 3(c) show an example of the stress fields σ_{yz} around a screw dislocation and σ_{xy} around an edge dislocation near the surface, respectively, generated by dislocation ($\boldsymbol{\sigma}^{\mathrm{D}}$), the correction stress fields ($\boldsymbol{\sigma}^{\mathrm{C}}$), and the superimposed stress fields ($\boldsymbol{\sigma}^{\mathrm{D}} + \boldsymbol{\sigma}^{\mathrm{C}}$). In the dislocation stress field, the stress on the surface is not zero, which implies that the surface traction is also not zero. Therefore, by superimposing it and the correction stress field, the stress on the surface can be zero.

The position of each dislocation where the force $\boldsymbol{f}$ at any point becomes zero is calculated using DD to obtain the equilibrium width w_{eq} between the two partial BPDs. By calculating the equilibrium distance w_{eq} at various depths d from the surface, partial dislocation pair types, such as 30°-30° and 30°-90°, and other geometrical conditions, we can elucidate the surface effect on the contraction of partial BPD pairs. Notably, we don't implement the effects of the C and Si cores in this study. The difference between the C and Si core mobilities does not significantly affect the overall trend, although the final shape of the dislocation pair may slightly vary. In addition, we don't consider the temperature effect, as the present analysis focuses on the static equilibrium configuration rather than the time evolution of dislocation behavior.

III. INFLUENCE OF THE TERRACE

A. Modeling

First, we employed the two-dimensional model shown in Fig. 4 to calculate the effect of terraces on the partial dislocation pair configurations. The stacking fault energy was set to 15 mJ/m^2, which was adopted as a

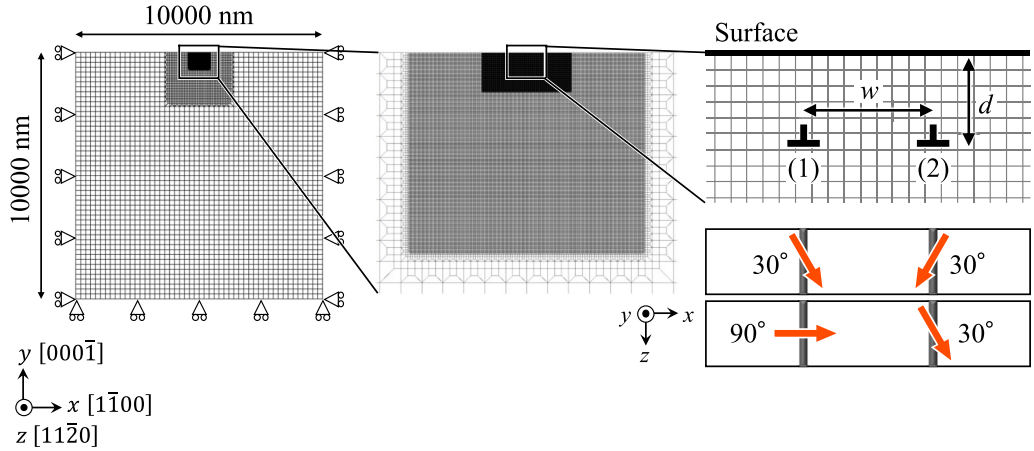


FIG. 4. Schematic of our two-dimensional model. Dislocations (1) and (2), with width w were set below a distance $d = 1, 2, \ldots, 100$ nm. Red arrows indicate the Burgers vectors of the dislocations; the types of dislocation pairs were 30°-30° and 90°-30°. A 10 000 nm × 10 000 nm finite element mesh, which has a fine mesh near the surface, was prepared to calculate the correction stress.

representative value considering previous experimental [39] ($14.7 \pm 2.5\,\mathrm{mJ/m^2}$) and first-principles calculation [40,41] (approximately 12–18 $\mathrm{mJ/m^2}$) results. The elastic constants were set to $C_{11} = 501$ GPa, $C_{12} = 111$ GPa, $C_{13} = 52$ GPa, $C_{33} = 553$ GPa, and $C_{44} = 163$ GPa [49]. A finite element mesh of 10 000 nm × 10 000 nm was prepared to calculate the correction stress field $\boldsymbol{\sigma}^{\mathrm{C}}$ generated by the surface, which was a sufficiently large model with fine meshes around the dislocations (less than 0.5 nm on each mesh side). We employed quadratic quadrilateral elements, and boundary conditions were set as shown in Fig. 4. The correction stress was calculated under plane strain conditions. We calculated the equilibrium dislocation widths w_{eq} at various depths from the surface between $d = 1$ and 100 nm using the method detailed in Sec. II. In addition, we calculated w_{eq} in a bulk environment by setting the correction stress to zero. We treated two types of partial BPDs: the 30°-30° and 30°-90° pairs, of which Burgers vector size was 0.1782 nm [50]. In these calculations, the dislocation width is taken as the equilibrium width w_{eq} when the force acting on each dislocation is less than 1.5×10^{-17} N/nm or the force difference from the previous dislocation dynamics step is less than 1.5×10^{-19} N/nm.

We also calculated the equilibrium width w_{eq} for various stacking fault energies. The results are provided in Appendix A.

B. Results

Figure 5 shows the relationship between the dislocation depth d from the surface and the equilibrium width w_{eq} between the dislocation pairs. Regarding the 30°-30° partial BPD pair, the equilibrium width w_{eq} at $d = 50$ nm was 25.1 nm. Therefore, the surface had almost no effect on the 30°-30° pair approximately 50 nm below the surface because the equilibrium width w_{eq} in a bulk, was calculated to be 25.9 nm. When a dislocation pair exists at a depth of less than $d = 50$ nm, the equilibrium width w_{eq} decreases significantly as the dislocation pair approaches the surface. The equilibrium width w_{eq} at a depth of $d = 2$ nm was 4.7 nm. Therefore, the 30°-30° pair dislocations can contract easily near the surface. Our results are consistent with the MD results in a previous study [37] and the BPD-TED conversion mechanism [19,21,43]. This is attributed to the greater effect of image forces derived from the surface, which are mainly attractive forces between the two dislocations, as discussed in the next section.

Regarding the 30°-90° partial BPD pair, the equilibrium width w_{eq} decreased as the depth d decreased. Notably, compared with the 30°-30° partial BPD pairs, the equilibrium width w_{eq} changed irregularly: it decreased slowly at $d > 25$ nm, became almost constant at $15 < d < 25$ nm, and then decreased significantly at $d < 15$ nm. The irregular changes are detailed subsequently. The equilibrium width w_{eq} at $d = 100$ nm was 36.2 nm, whereas that in a bulk was 38.3 nm. Therefore, the surface influences the deeper 30°-90°

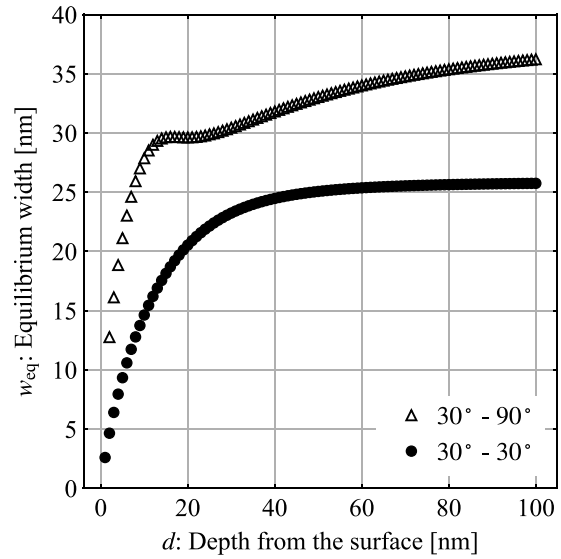


FIG. 5. Relationship between the depth d from the surface and the equilibrium width w_{eq} between two partial dislocations. The result at $d = 1$ nm in the 30°-90° partial BPD pair is unavailable owing to numerical instability.

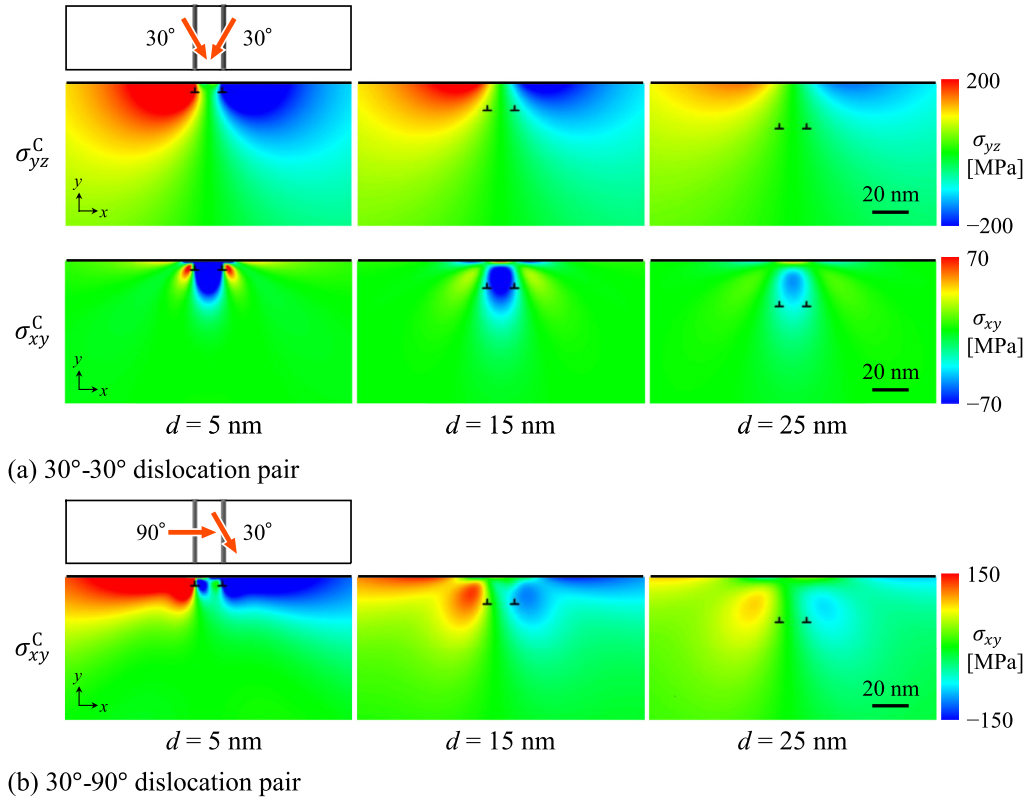


FIG. 6. Correction stress fields of (a) σ^{C}_{yz} and σ^{C}_{xy} around the 30°-30° dislocation pair and (b) σ^{C}_{xy} around the 30°-90° dislocation pair. The partial dislocation pair has a width of $w = 15.0$ nm and is located $d = 5$, 15, and 25 nm below the surface.

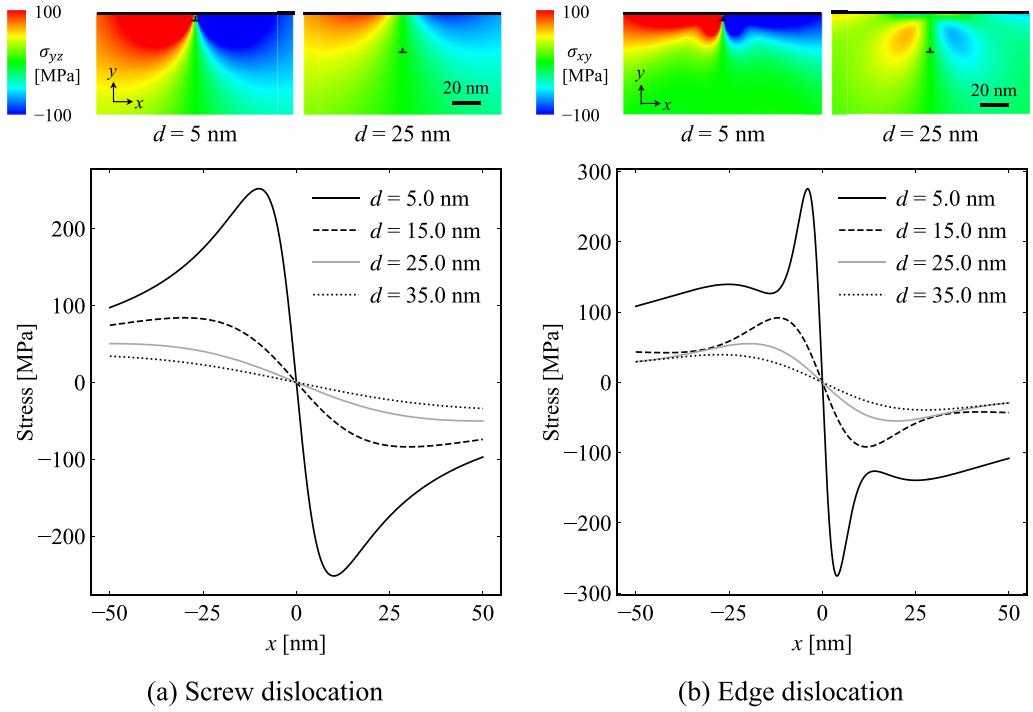
partial BPD pairs compared with the 30°-30° pairs. Moreover, the equilibrium widths of the 30°-90° partial BPD pairs are larger than those of the 30°-30° pairs at any depth d. For instance, the equilibrium width w_{eq} at $d = 2$ nm was 12.8 nm, which is approximately three times larger than that for the 30°-30° partial BPD pair. Therefore, the 30°-90° partial BPD pairs cannot contract more easily, even near the surface, than the 30°-30° partial BPD pairs.

C. Discussion

We discuss our results by comparing the correction stress fields generated by the surface because they cause surface effects according to Eq. (4). Figure 6(a) shows the correction stress fields of σ^{C}_{xy} and σ^{C}_{yz} at $d = 5$, 15, and 25 nm around a 30°-30° dislocation pair of $w = 15.0$ nm. Since the screw components of the Burgers vectors of the two partial dislocations are both positive, and the stress field σ^{C}_{yz} is positive at dislocation (1) and negative at dislocation (2), the Peach-Koehler forces acting on dislocations (1) and (2) are directed in the positive and negative directions, respectively. Consequently, an attractive interaction is generated between the two dislocations. The attractive force increases as the dislocation pair approaches to the surface because the magnitude of the stress σ^{C}_{yz} on the dislocation increases. Conversely, in the stress field σ^{C}_{xy}, the repulsive force between them increases as the dislocation pair gets close to the surface. Since the norm of the stress σ^{C}_{yz} is larger than that of the stress σ^{C}_{xy}, and the size of the Burgers vector b_z in the screw direction is larger than that of the Burgers vector b_x in the edge direction, the stress field σ^{C}_{yz} mainly affects the force between the two dislocations. Therefore, a larger attractive force causes the equilibrium width w_{eq} to decrease as the dislocation pair approaches the surface.

Figure 6(b) shows the correction stress field of σ^{C}_{xy} at $d = 5$, 15, and 25 nm around a 30°-90° dislocation pair with $w = 15.0$ nm. The attractive force between the two dislocations increases as the dislocation pair approaches the surface, because the stress on the dislocation increases. Therefore, similar to the 30°-30° dislocation pair, a larger attractive force causes the equilibrium width w_{eq} to decrease as the dislocation pair approaches the surface. Notably, we do not need to focus on the stress field σ^{C}_{yz} because it does not generate any force owing to the 90° partial dislocation, which is a complete edge dislocation.

For a more detailed discussion, we consider the correction stress field of one dislocation because the surface-derived Peach-Koehler force acting on a dislocation is caused by the correction stress of the other dislocation alone. In other words, the force is not generated by its own correction stress because the correction stress fields of one dislocation have a symmetrical distribution, as shown in Figs. 3(b) and 3(c). Figure 7(a) shows the relationship between the distance from a screw dislocation and the stress σ^{C}_{yz} at various depths from the surface. The correction stress fields σ^{C}_{yz} around the dislocation are also shown. The correction stress dislocation increases rapidly in the x range of 30 nm from it as d decreases. Therefore, for the 30°-30° dislocation pair, which primarily comprises screw dislocations, the attractive force between the two dislocations increases rapidly as it approaches the surface, resulting in

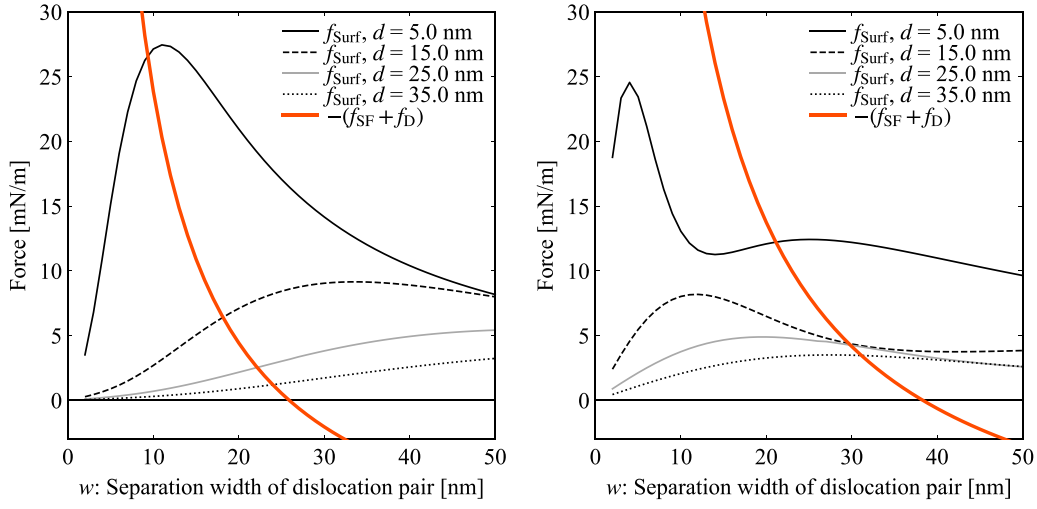


(a) Screw dislocation (b) Edge dislocation

FIG. 7. Relationship between the distance x from the dislocation and the correction stress for (a) screw and (b) edge dislocations at $d = 5$, 15, 25, and 35 nm. The correction stress fields are also shown for $d = 5$ and 25 nm.

a rapid decrease in the equilibrium width w_{eq}. Conversely, Fig. 7(b) shows the relationship between the distance from an edge dislocation and the stress σ_{xy}^{C}. Unlike a screw dislocation, several stress peaks are observed in the stress field. Thus, the stress around the dislocation increases irregularly as d decreases. This can result in the irregular decrease in the equilibrium width w_{eq}, as shown in Fig. 5.

Finally, Fig. 8 shows the relationships between the separation width of the dislocation pair and the force acting on dislocation (1) (shown in Fig. 2) in the (a) 30°-30° and (b) 30°-90° dislocation pairs at various depths d from the surface. Here, f_{PK} is decomposed into f_{D} and f_{Surf}, derived from $\boldsymbol{\sigma}^{\mathrm{D}}$ and $\boldsymbol{\sigma}^{\mathrm{C}}$, respectively. As $f_{\mathrm{SF}} + f_{\mathrm{PK}} = f_{\mathrm{SF}} + f_{\mathrm{D}} + f_{\mathrm{Surf}}$ in Eq. (1) becomes zero in the equilibrium width, the separation width at the intersection of lines $-(f_{\mathrm{SF}} + f_{\mathrm{D}})$ and f_{Surf} is equivalent to the equilibrium width w_{eq}. For example, the equilibrium widths for $d = 5$, 15, 25, and 35 nm obtained from Fig. 5 are 9.3, 18.1, 22.1, and 24.0 nm, respectively. The intersections of f_{Surf} and $-(f_{\mathrm{SF}} + f_{\mathrm{D}})$ in Fig. 8(a) are located at these values. The equilibrium width of the 30°-30° dislocation pair decreases rapidly as it approaches the surface, whereas that of the 30°-90° dislocation pair decreases



(a) (b)

FIG. 8. Relationship between the separation width of the dislocation pair and the force f_{Surf} and $-(f_{\mathrm{SF}} + f_{\mathrm{D}})$ acting on dislocation (1) at $d = 5.0$, 15.0, 25.0, and 35.0 nm. (a) 30°-30° partial dislocation pair. (b) 30°-90° partial dislocation pair.

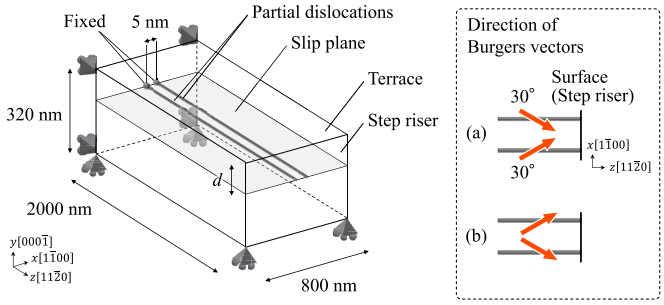


FIG. 9. Schematic of our three-dimensional model. A pair of 30°-30° BPDs was set on the slip plane. The finite element mesh with quadratic tetrahedral elements was set similarly to our two-dimensional model to calculate the effect of the surface on the dislocations. There are two types of Burgers vectors: (a) closed toward the surface (step riser) and (b) open toward it.

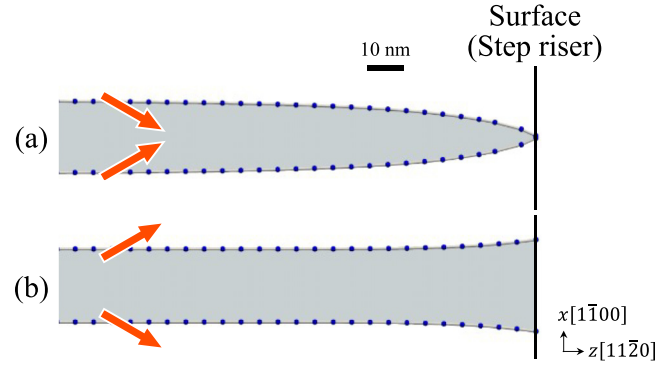


FIG. 10. BPD configurations at $d = 25$ nm. The results of two types of Burgers vectors [(a) closed toward the off-angle surface and (b) open toward the step riser] are shown. The gray lines and blue points indicate the dislocation lines and computational nodes, which are used for DD calculations, respectively. The gray area indicates the stacking fault between two BPDs.

irregularly owing to the irregularities in the stress field of an edge dislocation.

IV. INFLUENCE OF THE STEP RISER

A. Modeling

Next, we introduced a three-dimensional model to reproduce BPDs and discuss the influence of the step riser on BPD contraction. Figure 9 shows the schematic of our model. A pair of BPDs was set on a basal plane at depths ranging from $d = 1$ nm and $d = 25$ nm below the terrace. In addition, we employed $d = 60$ nm to reproduce the condition that the terrace has no effects on the BPDs. One end of the BPD is on a free surface (step riser), whereas the other is constrained. We employed a 30°-30° partial BPD pair with two types of Burgers vectors, closed and open, toward the step riser. In this simulation, we employed isotropic material properties because anisotropic and isotropic materials have nearly identical results in the two-dimensional simulation, as shown in Appendix B. The modulus of shearing elasticity and the Poisson's ratio were set to 194 GPa and 0.16, respectively [49]. The equilibrium configuration of the BPD pair was calculated using this model. We employed the parametric DD method [51] for our three-dimensional model, in which the dislocation lines are discretized into a series of segments with nodes at their endpoints, and the force acting on each segment is calculated using numerical integration.

B. Results

Figure 10 shows the BPD configurations, where the Burgers vectors are (a) closed and (b) open toward the step riser at $d = 25$ nm. The BPD pairs are constricted near the step riser in the closed Burgers vector results, whereas they are not constricted in those of the open Burgers vectors, as discussed later. Figure 11 shows the relationship between the distance l in the z direction from the step riser and the separation width w of the BPDs. In both results of the Burgers vector types, the partial BPD widths w decreased as the depth d decreased owing to the large image force near the terrace, as indicated in Sec. III. Notably, a significant difference was observed between the Burgers vector types. For the BPD pair with closed Burgers vectors [Fig. 11(a)], the BPD pairs were significantly constricted near the step riser. Conversely, the BPD pairs with open Burgers vectors [Fig. 11(b)] were not constricted. Moreover, we found that the x-directional deflection of the dislocation pair with an open Burgers vector is smaller than that of the dislocation pair with a closed Burgers vector. Thus, the BPD pair with closed Burgers vectors can contract more easily than that with open Burgers vectors. This difference is caused by the stress generated by the step riser, as discussed later.

In addition, the distance l, over which the step riser has an effect, decreases as the depth d from the terrace decreases. For instance, the effect of the step riser was within 10 nm for the BPD pair with closed Burgers vectors at $d = 1$ nm, whereas it was over 100 nm for $d = 25$ nm. Similarly, the effects of the step riser were within 20 and 60 nm for the BPD pair with open Burgers vectors at $d = 1$ and 25 nm, respectively. Therefore, the BPD pair with open Burgers vectors can contract at a certain distance from the step riser.

C. Discussion

The influence of the step riser on the BPD configurations near it is attributed to the stress field generated by the step riser. In our discussion, we decompose the stress field around a single 30° partial dislocation into edge and screw components. Figure 12 shows the correction stress fields σ_{yz}^{C} and σ_{xy}^{C} around (a) an edge dislocation and (b) a screw dislocation when the depth from the terrace is $d = 60$ nm. We observed two characteristic stress fields, which are crucial to BPD configurations near the step riser: the stress fields σ_{yz}^{C} and σ_{xy}^{C} derived from edge and screw dislocations, respectively.

First, we considered the force acting on a partial dislocation derived from the stress field generated by itself. Because the stress σ_{yz}^{C} derived from the edge component on the dislocation line is positive, the force in the positive-x direction acts on the screw component of the dislocation as shown in Fig. 13. Therefore, the contractive and expansive forces, respectively act on the dislocation pair with closed and open Burgers vectors. Notably, no effects on the dislocation derived

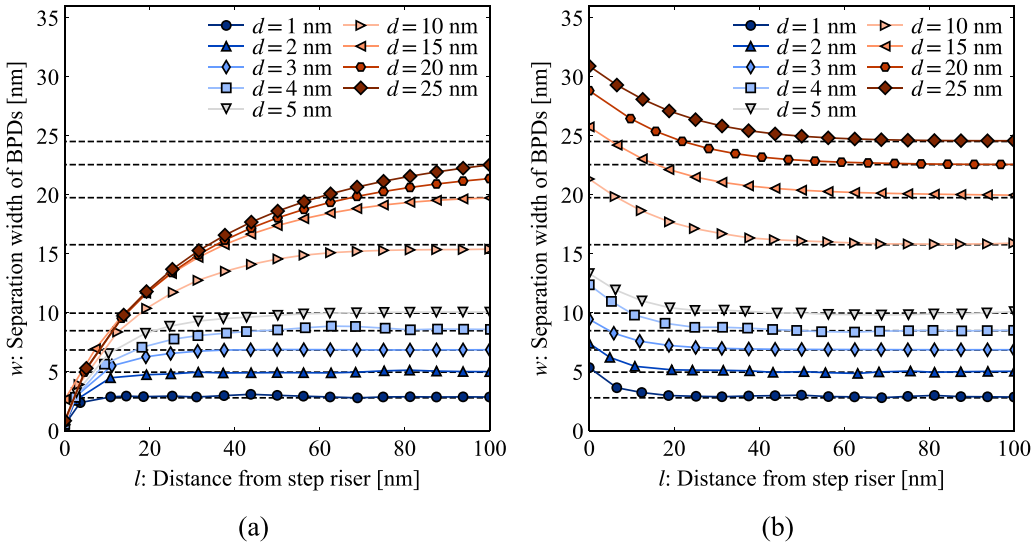


FIG. 11. Relationship between the distance from the step riser l and the separation width of the BPD pair w at depths ranging from d = 1–25 nm when the Burgers vectors are (a) closed toward the step riser and (b) open toward it. The dotted lines indicate the equilibrium width at each depth calculated in Sec. III.

from the other stress components generated by itself were observed because the stress on the dislocation line was zero.

Next, we considered the stress field of one dislocation and the direction of the force acting on its paired dislocation. Figure 14(a) shows the correction stress field around the edge dislocation and the force directions acting on its paired partial dislocation. The stress fields σ_{yz}^{C} and σ_{xy}^{C} act on the screw and edge components of the paired dislocation, respectively. If the paired dislocation lies on the positive-x side of the edge dislocation [Fig. 14(a), left], which corresponds to the closed Burgers vectors, then the expansive force acts on the screw component of the paired dislocation near the step riser. Conversely, if the paired dislocation lies on the negative-x side of the edge dislocation [Fig. 14(a), right], which corresponds to the open Burgers vectors, then a contractive force acts on the screw component of the paired dislocation near the step riser. The force acting on the edge component of the paired dislocation does not depend on the type of Burgers vector. We should note that the edge dislocation generates both positive and negative stress σ_{xy}^{C} [Fig. 12(a)]. Therefore, the direction of the force acting on the edge component of the paired dislocation depends on the position. Near the surface, the force acts in the contraction direction, whereas away from the surface, it acts in the expansion direction.

Figure 14(b) shows the correction stress field around the screw dislocation and force directions acting on the paired partial dislocation. If the paired dislocation lies on the positive-x side of the screw dislocation [Fig. 14(b), left], then the contractive force acts on the screw component of the paired dislocation near the surface, affecting both Burgers vector types. When the direction of the edge component of the paired dislocation is positive, corresponding to open Burgers vectors, an expansive force acts on it. Conversely, when its direction is negative, corresponding to the closed Burgers vectors, the contractive force acts on it. Similarly, if the paired

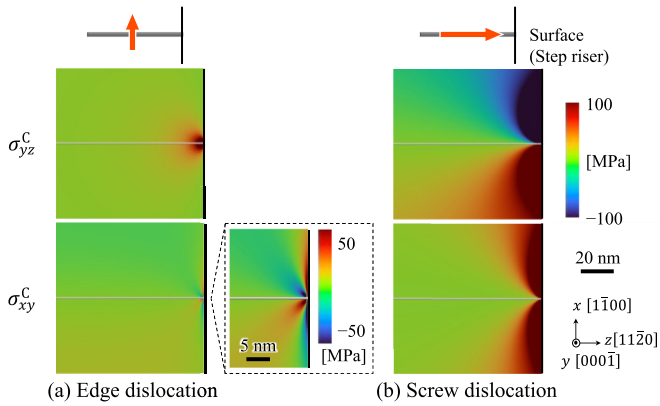


FIG. 12. Correction stress fields σ_{yz}^{C} and σ_{xy}^{C} around (a) an edge dislocation and (b) a screw dislocation when the depth from the terrace is d = 60 nm. The enlarged figure of σ_{xy}^{C} generated from the edge dislocation is also indicated.

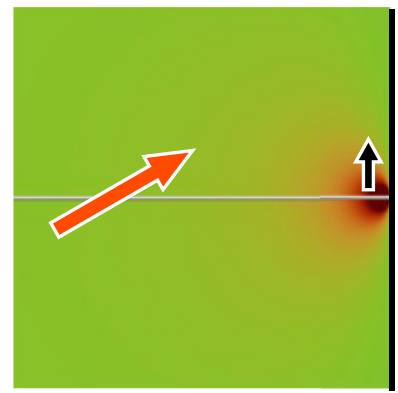


FIG. 13. Correction stress field σ_{yz}^{C} derived from the edge components. The red and black arrows indicate the Burgers vector and force acting on the screw component, respectively.

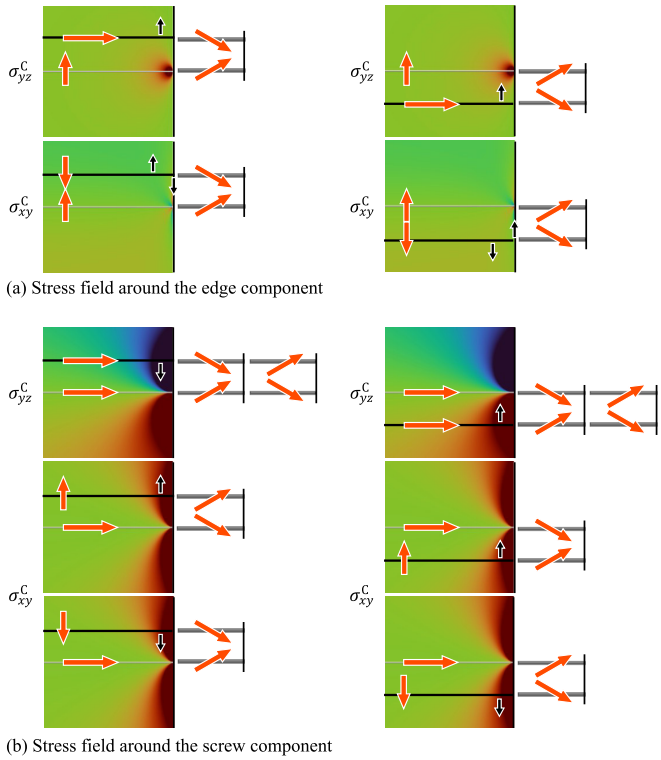


FIG. 14. Correction stress fields around one dislocation (gray solid line) derived from the (a) edge and (b) screw components. Forces acting on its paired partial dislocation (black dotted line) are also shown by black arrows. The red arrows indicate the Burgers vectors. The schematic to the right of each contour represents the corresponding partial dislocation pair.

dislocation lies on the negative-x side of the screw dislocation [Fig. 14(b), right], then the contractive and expansive forces act on the edge component of the paired dislocation when the Burgers vector types are closed and open, respectively.

Therefore, the stress fields σ^C_{yz} and σ^C_{xy} around the edge and screw dislocations, respectively, cause the dependence of the Burgers vector types on the BPD configurations near the step riser. Because the area and magnitude of the latter stress field [σ^C_{xy} in Fig. 14(b)] are significantly larger than those of the former [σ^C_{yz} in Fig. 14(a)], the contractive force acts on the BPD pair with closed Burgers vectors while the expansive force acts on that with open Burgers vectors. Moreover, the contractive force derived from σ^C_{yz} around a screw dislocation [σ^C_{yz} in Fig. 14(b)] makes the x-directional deflection of the dislocation pair with a closed Burgers vector larger compared with that with an open Burgers vector.

Figure 15 shows the σ^C_{yz} and σ^C_{xy} stress fields around edge and screw dislocations, respectively, at various depths from the terrace ($d = 5$, 15, and 25 nm). No effects of the depth d on σ^C_{yz} stress field are observed. However, the distribution of the stress field σ^C_{xy} decreases as the depth d decreases, resulting in a smaller effect of the step riser compared with the effect of the terrace. This is attributed to the larger image force derived from the terrace, as discussed in Sec. III.

Our discussion can also predict the movements of the 30°-90° partial BPD pairs. The edge components of the 30°

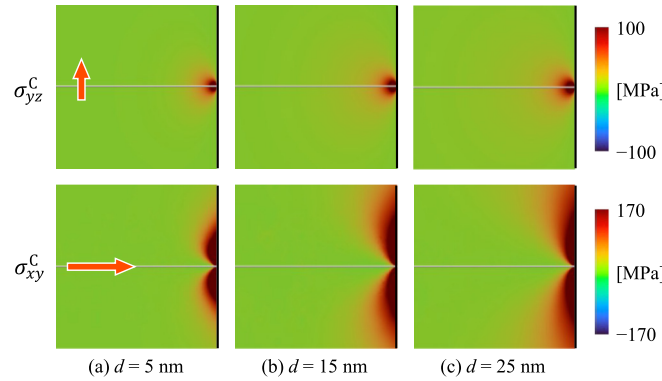


FIG. 15. σ^C_{yz} and σ^C_{xy} stress fields around edge and screw dislocations, respectively, when the depths at terrace depths of (a) $d = 5$ nm, (b) $d = 15$ nm, and (c) $d = 25$ nm.

and 90° partial dislocations acting in the same direction will cause a notable behavior in the pair. Here, we consider the 30°-90° partial BPD pairs with Burgers vectors, as shown in Fig. 16(a). The stress field σ^C_{yz} derived from the 90° partial dislocation [Fig. 16(b)] and the edge component of the 30° partial dislocation [Fig. 16(c)] generates the positive-x direction force acting on the screw component of the 30° partial dislocation. Conversely, the stress field σ^C_{xy} derived from the screw component of the 30° partial dislocation generates the positive-x direction force acting on the 90° partial dislocation. Therefore, both the 30° and 90° partial dislocations are subjected to forces in the same direction. This implies that both partial dislocations moved in the same direction, and the 30°-90° partial BPD pairs were eliminated in the epitaxial layer owing to the step riser.

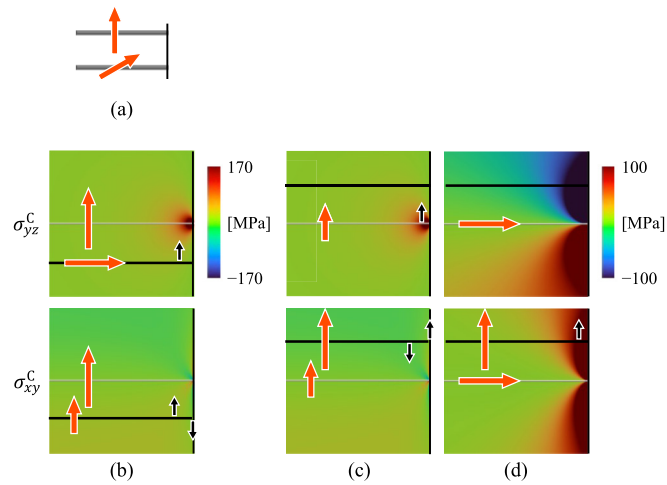


FIG. 16. Stress fields of a 30°-90° partial BPD pair. (a) Configuration of the BPD pair. (b) Stress field derived from the 90° partial BPD. (c) Stress field derived from the edge component of the 30° partial BPD. (d) Stress field derived from the screw component of the 30° partial BPD. The red and black arrows indicate the Burgers vectors and force acting on the dislocations, respectively.

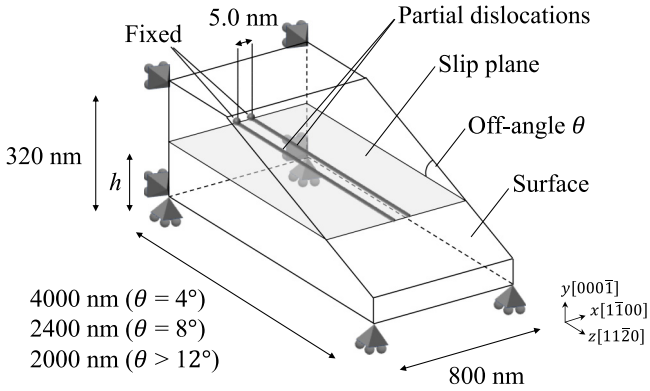


FIG. 17. Schematic of our three-dimensional model. A pair of 30°-30° BPD was set on the slip plane. The off-angle $\boldsymbol{\theta}$ was set to be 4°, 8°, 12°, and 16°. Finite element mesh was set like our two-dimensional model to calculate the effect of the surface on the dislocations.

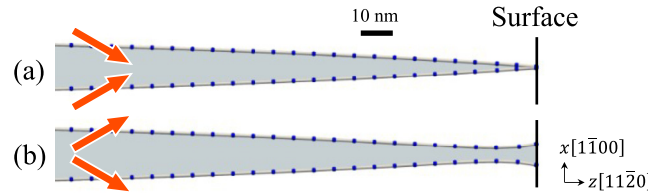


FIG. 18. BPD configurations at off-angle $\theta = 4°$. The results of the two types of Burgers vectors: (a) closed toward the off-angle surface and (b) open toward it, are shown. The gray lines and blue points indicate the dislocation lines and computational nodes, which are used for DD calculations, respectively. The gray area indicates the stacking fault between the two BPDs.

V. INFLUENCE OF THE OFF-ANGLE ON BPD CONTRACTION

A. Modeling

Finally, we introduced a three-dimensional model with an off-angle to discuss its effect on BPD contraction. Figure 17 shows the schematic of our model. A pair of BPDs was set on a basal plane. One end of the BPD is on a free surface with off-angle $\theta = 4°$, 8°, 12°, and 16° to the basal plane, whereas the other is constrained. We employed a 30°-30° partial BPD pair with two types of Burgers vectors, closed and open, toward the surface, as shown in Sec. IV. The equilibrium configuration of the BPD pair was calculated using the same method described in Sec. IV. The distance h between the slip plane and the bottom surface of the model is approximately half of the model height. The exact value varies slightly with the off-angle θ: $h = 185.7$, 176.6, 154.2, and 176.6 nm for $\theta = 4$, 8, 12, and 16°, respectively. Since the plane is sufficiently far from the top and bottom surfaces of the model, these differences are expected to have a negligible effect on dislocation motion. We should note that we did not model steps on the surface because a model with steps has a high computational cost owing to the extremely small elements required for the finite element method (FEM) to calculate the correction stress. The effects of modeling the steps are discussed in Appendix C.

B. Result and discussion

Figure 18 shows the BPD configurations, of which Burgers vectors are (a) closed and (b) open toward the off-angle surface at off-angle $\theta = 4°$. The BPD pair with closed Burgers vectors is constricted near the surface, whereas that with open Burgers vectors is constricted approximately 20 nm from the surface. This is attributed to the stress field generated by the surface, as discussed in Sec. IV. Figure 19 shows the relationship between the distance l in the z direction from the surface and the partial BPD width w. In the results of both Burgers vector types, the partial BPD widths w decreases as the off-angle θ decreases. This is consistent with our two-dimensional simulations because the distance from the surface decreases as the off-angle decreases. Therefore, the partial BPD pair can easily contract to a perfect one, which is a crucial process of BPD-TED conversion, in a low off-angle epitaxial layer. These results are consistent with those of previous studies [22,23].

A difference in the BPD pair configurations was observed between the Burgers vector types, attributed to the effect of the step riser discussed in Sec. IV. For the BPD pair with Burgers vectors closed toward the surface, the BPD pair is constricted near the surface. Thus, the BPD pair can easily contract to a perfect one. By contrast, for the BPD pair with open Burgers vectors toward the surface, it is constricted far from the surface. In addition, the BPD widths are larger than those of the closed Burgers vectors at any distance l from the surface and the off-angle θ. Therefore, it would be more difficult for the BPD pair to contract perfectly.

VI. CONCLUSIONS

We computationally elucidated the effect of the surface on the contraction of partial BPD pairs in 4H-SiC using DD. Our model can reproduce the force derived from their elastic interactions and stacking faults based on dislocation theories. In addition, we reproduced the forces derived from the surface, such as the image force, by adding the correction stress to our model to satisfy the condition that the surface traction t_i on the surface must be zero. Using our method, we calculated the partial BPD configurations in various models.

First, we focused on the effects of the terrace and step riser on the contraction of a BPD pair using two- and three-dimensional models, respectively. In the former simulation, we found that the equilibrium distance decreased as the depth decreased owing to the large correction stress, resulting in an increase in the attractive force between the dislocations. This indicates that partial BPDs can easily contract near the surface. In particular, the 30°-30° partial BPD pairs can contract more easily than the 30°-90° partial BPD pairs owing to their correction stress field. In the latter simulation, we found that the direction of the Burgers vectors of the dislocation has an effect on the partial BPD contraction owing to the correction field generated by the step riser: the BPD pair can contract easily when the two Burgers vectors are closed toward the surface but not when they are open.

Finally, we employed a model with an off-angle to clarify its effect. Our results showed that the BPD width for a

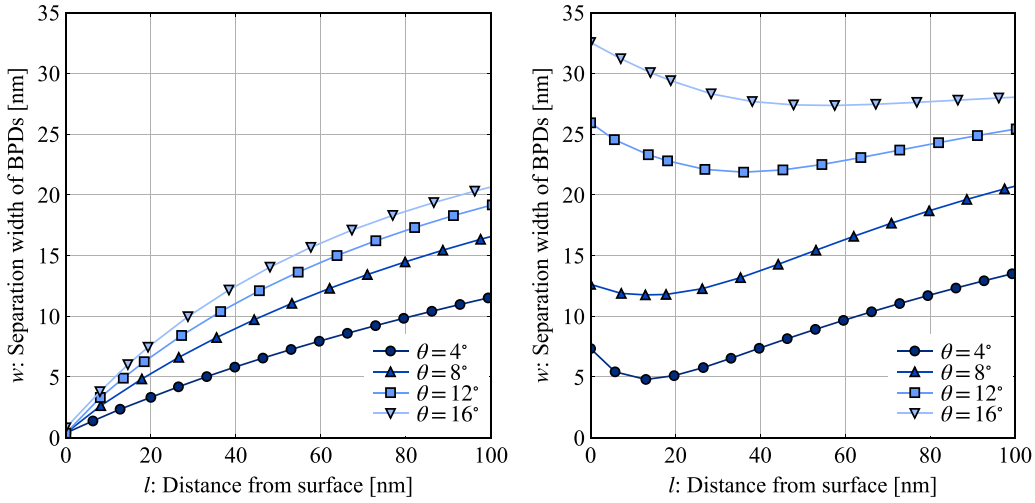


FIG. 19. Relationship between the distance l from the off-angle surface and the partial BPD width w for the Burgers vectors (a) closed and (b) open toward the off-angle surface. The plots indicate the computational nodes on the dislocations.

small off-angle decreased because the distance between the BPD and the surface decreased. Therefore, a small off-angle can lead to a high BPD-TED conversion rate, which is consistent with the experimental results. Moreover, our results indicate that BPDs with open Burgers vectors cannot easily contract.

Overall, our results elucidated the mechanism of the contraction of partial BPD pairs near the surface and the effect of the off-angle in their epitaxial layers based on dislocation theories. In particular, the direction of Burgers vector affects the contraction of the partial BPD pairs. Therefore, our results indicate that an effective approach for promoting the contraction of partial BPD pairs with open Burgers vectors is important to improve the BPD-TED conversion rate. In addition, our computational model is expected to be applicable to other conditions in the SiC epitaxy, and moreover, dislocation issues in other materials.

However, our results that the contractions depend on the direction of the Burgers vectors does not explain the reason why most BPDs are converted to TEDs. One possible reason is the absence of time evolution because our simulation calculates the equilibrium configuration of dislocations. Therefore, time-evolution simulation incorporating the effects of temperature and dislocation mobilities is required to provide further insight into the mechanism of the contractions of the partial BPD pairs, which cannot be fully captured by our present static simulation. Moreover, atomic effects, such as the finite extension of the dislocation core, may become important in the vicinity of the surface. Incorporating these effects into future simulation models is expected to enhance the predictive capability of the model.

ACKNOWLEDGMENT

This work was supported by JSPS KAKENHI Grant No. JP26K21238.

DATA AVAILABILITY

The data that support the findings of this article are not publicly available. The data are available from the authors upon reasonable request.

APPENDIX A: EFFECT OF STACKING FAULT ENERGY ON EQUILIBRIUM WIDTH

The stacking fault energy of SiC decreases because of the quantum well action mechanism [52], resulting in the expansion of the stacking fault [53,54]. Here, we calculated the equilibrium width between partial dislocations, which corresponds to the stacking fault area in the two-dimensional model, for various stacking fault energies.

Figure 20 shows the relationship between the depth d of the dislocations from the surface and the equilibrium width w_{eq} for the stacking fault energy of 5, 10, 15, and 20 mJ/m^2. In both 30°-30° and 30°-90° cases, w_{eq} greatly increases as the stacking fault energy decreases. The equilibrium widths of the 30°-30° partial BPD pairs in bulk for the stacking fault energies of 5, 10, 15, and 20 mJ/m^2 are 77.7, 38.9, 25.9, and 19.4 nm, respectively. This is attributed to smaller attractive forces between the dislocations derived from the stacking fault for smaller stacking fault energies. Therefore, the stacking fault energy can greatly affect the expansion of the stacking fault. Moreover, a smaller stacking fault energy requires a larger depth d for w_{eq} to reach its bulk value. Therefore, the influence of the surface becomes more significant for smaller stacking fault energy.

APPENDIX B: COMPARISON OF ISOTROPIC AND ANISOTROPIC MATERIAL MODELS

We calculated the equilibrium distance between the dislocations in our two-dimensional model for an isotropic material. The modulus of shearing elasticity and the Poisson's

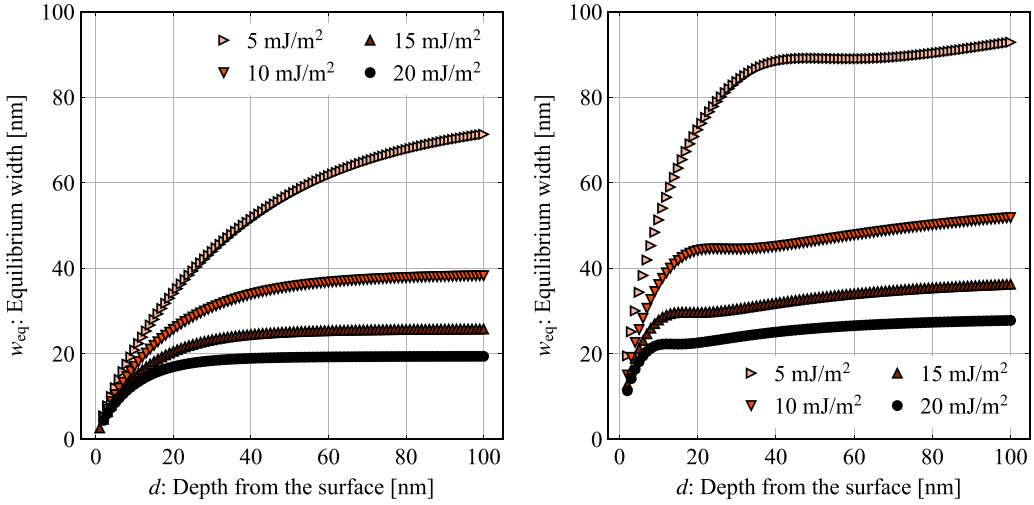


FIG. 20. Relationship between the depth d of the dislocations from the surface and the equilibrium distance w_{eq} for various stacking fault energies.

ratio were set to 194 GPa and 0.16, respectively. Figure 21 shows the relationship between the depth d of the dislocations from the surface and the equilibrium distance w_{eq}. The relationship for an isotropic material is nearly identical to that for an anisotropic material (Fig. 5), although the w_{eq} for an isotropic material is slightly larger than that for an anisotropic material. Therefore, we employed the material with isotropic properties for the three-dimensional simulation.

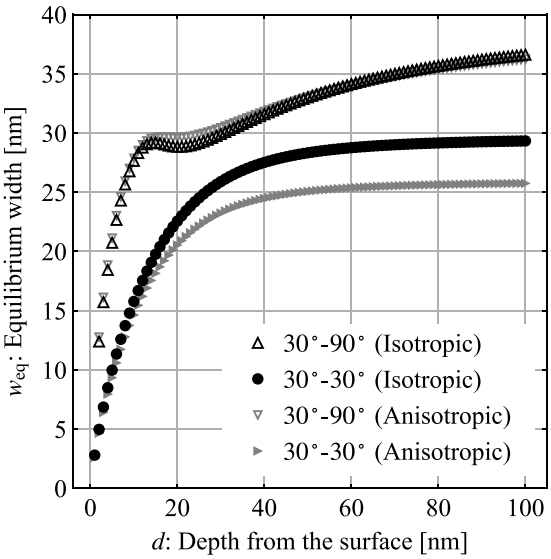


FIG. 21. Relationship between the depth d of the dislocations from the surface and the equilibrium distance w_{eq} for isotropic and anisotropic materials. The results for anisotropic material are identical to those in Fig. 5.

APPENDIX C: EFFECT OF SURFACE GEOMETRY ON THE BPD CONTRACTIONS

Because our model in Sec. V does not reproduce steps on the surface, our results may overestimate or underestimate the difficulty of the BPD contractions. Here, we calculated the configuration of the BPD pair near the surface by employing three models: (a) an off-angle model, (b) a step model, and (c) a step riser model, as shown in Fig. 22. The off-angle model is the same as that described in Sec. V. In the step model, we introduced one terrace and one step. Their length and height are 14.3 and 1.0 nm, respectively, which corresponds to an off-angle of 4°. The depth of the BPD pair from the terrace is $d = 1$ nm. The step riser model was the same as that at $d = 1$ nm in Sec. IV.

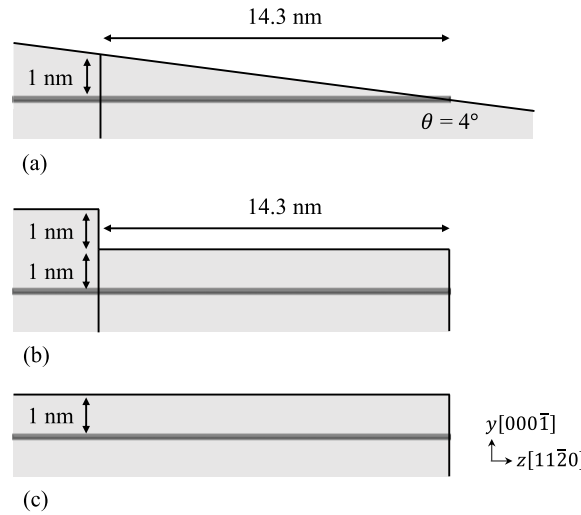


FIG. 22. Schematic of three models: (a) off-angle model, (b) step model, and (c) step riser model. The model size and boundary conditions are the same as those in the models in Secs. IV and V.

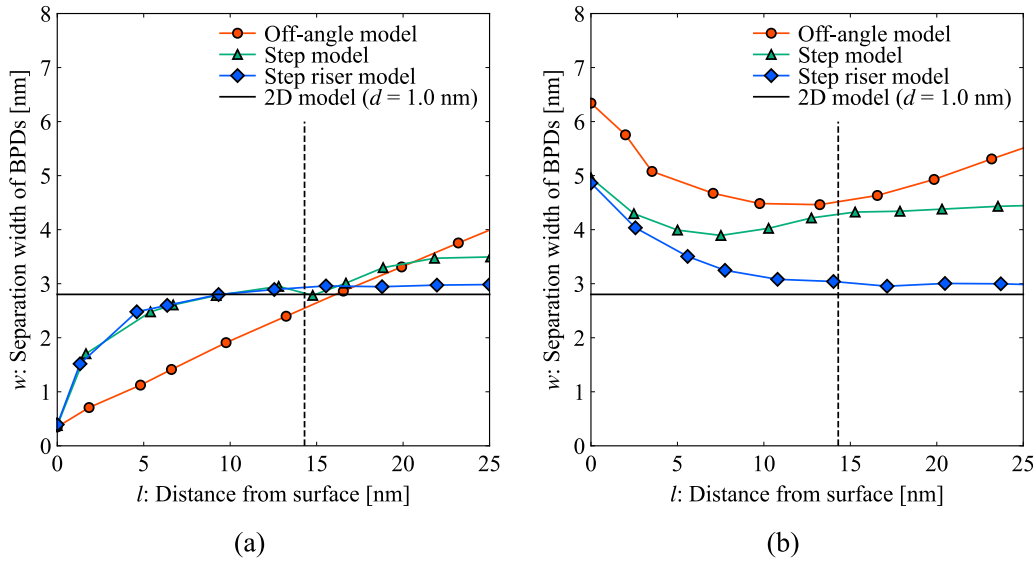


FIG. 23. Relationship between the distance l from the off-angle surface and the partial BPD width w for the Burgers vectors (a) closed and (b) open toward the off-angle surface. Plots indicate computational nodes on the dislocations.

Figure 23 shows the relationship between the distance l from the surface (step riser) and the separation width w of the BPD pair with (a) closed and (b) open Burgers vectors. The results of the two-dimensional model in Sec. III are also presented. In the results of the closed Burgers vectors, the widths in the step and step riser models are larger than those in the off-angle model because the depths from the surface in these models are larger than that in the off-angle model; the depths of the former are constantly 1 nm, whereas that of the latter is less than 1 nm for l in the range of 0–14.3 nm. However, this does not affect the contraction of the BPD pairs because the widths at $l = 0$ nm in all models are almost the same.

In the results of the open Burgers vectors, the width in the step is smaller ($w = 3.89$ nm at $l = 7.51$ nm) than that in the off-angle model ($w = 4.46$ nm at $l = 13.2$ nm). This is attributed to the effect of the stress field generated by the step riser described in Sec. IV: the effect becomes larger when the dislocation pair is placed near the surface. Although the width in the step model is larger than that in the step riser model owing to the effect of the upper step ($l > 14.3$ nm), in reality, the BPD pair can contract more easily than that in our simulation described in Sec. V.

[1] M. Bhatnagar and B. J. Baliga, Comparison of 6H-SiC, 3C-SiC, and Si for power devices, IEEE Trans. Electron Devices **40**, 645 (1993).

[2] J. A. Cooper and A. Agarwal, SiC power-switching devices-the second electronics revolution? Proc. IEEE **90**, 956 (2002).

[3] F. F. Wang and Z. Zhang, Overview of silicon carbide technology: Device, converter, system, and application, *in CPSS Transactions on Power Electronics and Applications* (IEEE, Piscataway, NJ, 2016), Vol. 1, pp. 13–32.

[4] H. Matsunami and T. Kimoto, Step-controlled epitaxial growth of SiC: High quality homoepitaxy, Mater. Sci. Eng.: Rep. **20**, 125 (1997).

[5] H. Matsunami, Technological breakthroughs in growth control of silicon carbide for high power electronic devices, Jpn. J. Appl. Phys. **43**, 6835 (2004).

[6] T. Kimoto, N. Miyamoto, and H. Matsunami, Performance limiting surface defects in SiC epitaxial p-n junction diodes, IEEE Trans. Electron Devices **46**, 471 (1999).

[7] R. Singh, Reliability and performance limitations in SiC power devices, Microelectron. Reliab. **46**, 713 (2006).

[8] T. Kimoto and H. Watanabe, Defect engineering in SiC technology for high-voltage power devices, Appl. Phys. Express **13**, 120101 (2020).

[9] P. G. Neudeck and J. A. Powell, Performance limiting micropipe defects in silicon carbide wafers, IEEE Electron Device Lett. **15**, 63 (1994).

[10] Y. Cui, J. Li, K. Zhou, X. Zhang, and G. Sun, Influence of extended defects and oval shaped facet on the minority carrier lifetime distribution in as-grown 4H-SiC epilayers, Diam. Relat. Mater. **92**, 25 (2019).

[11] D. Baierhofer, B. Thomas, F. Staiger, B. Marchetti, C. Förster, and T. Erlbacher, Defect reduction in SiC epilayers by different substrate cleaning methods, Mater. Sci. Semicond. Process. **140**, 106414 (2022).

[12] S. Izumi, H. Tsuchida, I. Kamata, and T. Tawara, Structural analysis and reduction of in-grown stacking faults in 4H-SiC epilayers, Appl. Phys. Lett. **86**, 202108 (2005).

[13] R. E. Stahlbush, B. L. VanMil, R. L. Myers-Ward, K.-K. Lew, D. K. Gaskill, and C. R. Eddy, Basal plane dislocation reduction in 4H-SiC epitaxy by growth interruptions, Appl. Phys. Lett. **94**, 041916 (2009).

[14] H. Tsuchida, M. Ito, I. Kamata, and M. Nagano, Formation of extended defects in 4H-SiC epitaxial growth and development of a fast growth technique, Physica Status Solidi (B) **246**, 1553 (2009).

[15] J. Senzaki, K. Kojima, T. Kato, A. Shimozato, and K. Fukuda, Correlation between reliability of thermal oxides and dislocations in n-type 4H-SiC epitaxial wafers, Appl. Phys. Lett. **89**, 022909 (2006).

[16] M. Skowronski and S. Ha, Degradation of hexagonal silicon-carbide-based bipolar devices, J. Appl. Phys. **99**, 011101 (2006).

[17] T. Ueda, H. Nishino, and H. Matsunami, Crystal growth of SiC by step-controlled epitaxy, J. Cryst. Growth **104**, 695 (1990).

[18] T. Kimoto, A. Iijima, H. Tsuchida, T. Miyazawa, T. Tawara, A. Otsuki, T. Kato, and Y. Yonezawa, Understanding and reduction of degradation phenomena in SiC power devices, in *Proceedings of the IEEE International Reliability Physics Symposium (IRPS)* (IEEE, Piscataway, NJ, 2017), pp. 2A-1.1–2A-1.7

[19] S. Chung, V. Wheeler, R. Myers-Ward, C. R. Eddy, D. K. Gaskill, P. Wu, Y. N. Picard, and M. Skowronski, Direct observation of basal-plane to threading-edge dislocation conversion in 4H-SiC epitaxy, J. Appl. Phys. **109**, 094906 (2011).

[20] S. Ha, P. Mieszkowski, M. Skowronski, and L. B. Rowland, Dislocation conversion in 4H silicon carbide epitaxy, J. Cryst. Growth **244**, 257 (2002).

[21] T. Ohno, H. Yamaguchi, S. Kuroda, K. Kojima, T. Suzuki, and K. Arai, Direct observation of dislocations propagated from 4H-SiC substrate to epitaxial layer by x-ray topography, J. Cryst. Growth **260**, 209 (2004).

[22] R. Myers-Ward, D. K. Gaskill, R. S. Stahlbush, N. A. Mahadik, V. Wheeler, L. O. Nyakiti, and C. R. Eddy, Managing basal plane dislocations in SiC: Perspective and prospects, ECS Trans. **50**, 103 (2013).

[23] W. Chen and M. A. Capano, Growth and characterization of 4H-SiC epilayers on substrates with different off-cut angles, J. Appl. Phys. **98**, 114907 (2005).

[24] B. L. VanMil, R. E. Stahlbush, R. L. Myers-Ward, K.-K. Lew, C. R. Eddy, and D. K. Gaskill, Basal plane dislocation reduction for 8° off-cut, 4H-SiC using *in situ* variable temperature growth interruptions, J. Vac. Sci. Technol. B **26**, 1504 (2008).

[25] T. Hori, K. Danno, and T. Kimoto, Fast homoepitaxial growth of 4H-SiC with low basal-plane dislocation density and low trap concentration by hot-wall chemical vapor deposition, J. Cryst. Growth **306**, 297 (2007).

[26] X. Zhang and H. Tsuchida, Conversion of basal plane dislocations to threading edge dislocations in 4H-SiC epilayers by high temperature annealing, J. Appl. Phys. **111**, 123512 (2012).

[27] A. Balachandran, T. S. Sudarshan, and M. V. S. Chandrashekhar, Basal plane dislocation free recombination layers on low-doped buffer layer for power devices, Cryst. Growth Des. **17**, 1550 (2017).

[28] H. Song, T. Rana, and T. S. Sudarshan, Investigations of defect evolution and basal plane dislocation elimination in CVD epitaxial growth of silicon carbide on eutectic etched epilayers, J. Cryst. Growth **320**, 95 (2011).

[29] Z. Zhang and T. S. Sudarshan, Basal plane dislocation-free epitaxy of silicon carbide, Appl. Phys. Lett. **87**, 151913 (2005).

[30] R. L. Myers-Ward, N. A. Mahadik, V. D. Wheeler, L. O. Nyakiti, R. E. Stahlbush, E. A. Imhoff, K. D. Hobart, C. R. Eddy, and D. K. Gaskill, Spontaneous conversion of basal plane dislocations in 4° off-axis 4H-SiC epitaxial layers, Cryst. Growth Des. **14**, 5331 (2014).

[31] G. Savini, M. I. Heggie, and S. Öberg, Core structures and kink migrations of partial dislocations in 4H-SiC, Farad. Discuss. **134**, 353 (2007).

[32] P. K. Sitch, R. Jones, S. Öberg, and M. I. Heggie, *Ab initio* investigation of the dislocation structure and activation energy for dislocation motion in silicon carbide, Phys. Rev. B **52**, 4951 (1995).

[33] A. T. Blumenau, C. J. Fall, R. Jones, S. Öberg, T. Frauenheim, and P. R. Briddon, Structure and motion of basal dislocations in silicon carbide, Phys. Rev. B **68**, 174108 (2003).

[34] A. T. Blumenau, C. J. Fall, R. Jones, M. I. Heggie, P. R. Briddon, T. Frauenheim, and S. berg, Straight and kinked 90° partial dislocations in diamond and 3C-SiC, J. Phys. Condens. Matter **14**, 12741 (2002).

[35] T. A. G. Eberlein, R. Jones, A. T. Blumenau, S. Öberg, and P. R. Briddon, Movement and pinning of dislocations in SiC, Physica Status Solidi (C) **4**, 2923 (2007).

[36] Y. Tamura, H. Sakakima, S. Takamoto, A. Hatano, and S. Izumi, Reaction pathway analysis for the conversion of perfect screw basal plane dislocation to threading edge dislocation in 4H-SiC, Jpn. J. Appl. Phys. **58**, 081005 (2019).

[37] A. Hirano, H. Sakakima, A. Hatano, and S. Izumi, Charge-transfer interatomic potential to reproduce 30° partial dislocation movements for 4H-SiC in the surface vicinity and its application to BPD-TED conversion, Comput. Mater. Sci. **231**, 112588 (2024).

[38] A. Hirano, H. Sakakima, A. Hatano, and S. Izumi, Effects of terraces and steps on the 4H-SiC BPD-TED conversion rate: A reaction pathway analysis, J. Appl. Phys. **135**, 095701 (2024).

[39] M. H. Hong, A. V. Samant, and P. Pirouz, Stacking fault energy of 6H-SiC and 4H-SiC single crystals, Philos. Mag. A **80**, 919 (2000).

[40] H. Sakakima, S. Takamoto, A. Hatano, and S. Izumi, Temperature-dependent stacking fault energies of 4H-SiC: A first-principles study, J. Appl. Phys. **127**, 125703 (2020).

[41] H. Sakakima, A. Hatano, and S. Izumi, Comparative study of the effect of van der Waals interactions on stacking fault energies in SiC, J. Appl. Phys. **130**, 215701 (2021).

[42] J. L. Demenet, X. Milhet, and J. Rabier, TEM observations of the coexistence of perfect and dissociated dislocations in SiC under high stress, Physica Status Solidi (C) **2**, 1987 (2005).

[43] N. Zhang, Y. Chen, Y. Zhang, M. Dudley, and R. E. Stahlbush, Nucleation mechanism of dislocation half-loop arrays in 4H-silicon carbide homoepitaxial layers, Appl. Phys. Lett. **94**, 122108 (2009).

[44] T. A. Khraishi and H. M. Zbib, Free-surface effects in 3D dislocation dynamics: Formulation and modeling, J. Eng. Mater. Technol. **124**, 342 (2002).

[45] A. B. Siddique and T. Khraishi, Numerical methodology for treating static and dynamic dislocation problems near a free surface, J. Phys. Commun. **4**, 055005 (2020).

[46] M. C. Fivel, T. J. Gosling, and G. R. Canova, Implementing image stresses in a 3D dislocation simulation, Model. Simul. Mat. Sci. Eng. **4**, 581 (1996).

[47] M. C. Fivel and G. R. Canova, Developing rigorous boundary conditions to simulations of discrete dislocation dynamics, Model. Simul. Mat. Sci. Eng. **7**, 753 (1999).

[48] H. Jacobson, J. Birch, R. Yakimova, M. Syväjärvi, J. P. Bergman, A. Ellison, T. Tuomi, and E. Janzén, Dislocation

evolution in 4H-SiC epitaxial layers, J. Appl. Phys. **91**, 6354 (2002).

[49] K. Kamitani, M. Grimsditch, J. C. Nipko, C.-K. Loong, M. Okada, and I. Kimura, The elastic constants of silicon carbide: A Brillouin-scattering study of 4H and 6H SiC single crystals, J. Appl. Phys. **82**, 3152 (1997).

[50] M. Iuga, G. Steinle-Neumann, and J. Meinhardt, *Ab-initio* simulation of elastic constants for some ceramic materials, Eur. Phys. J. B **58**, 127 (2007).

[51] N. M. Ghoniem, S.-H. Tong, and L. Z. Sun, Parametric dislocation dynamics: A thermodynamics-based approach to investigations of mesoscopic plastic deformation, Phys. Rev. B **61**, 913 (2000).

[52] A. Iijima and T. Kimoto, Electronic energy model for single Shockley stacking fault formation in 4H-SiC crystals, J. Appl. Phys. **126**, 105703 (2019).

[53] T. A. Kuhr, J. Liu, H. J. Chung, M. Skowronski, and F. Szmulowicz, Spontaneous formation of stacking faults in highly doped 4H-SiC during annealing, J. Appl. Phys. **92**, 5863 (2002).

[54] M. S. Miao, S. Limpijumnong, and W. R. L. Lambrecht, Stacking fault band structure in 4H-SiC and its impact on electronic devices, Appl. Phys. Lett. **79**, 4360 (2001).